DISENTANGLING BARYONS AND DARK MATTER IN THE SPIRAL GRAVITATIONAL LENS B1933+503

S. H. Suyu[1,2,3], S. W. Hensel[3,4], J. P. McKean[5], C. D. Fassnacht[6], T. Treu[1,13], A. Halkola[7], M. Norbury[8], N. Jackson[9],
P. Schneider[3], D. Thompson[10], M. W. Auger[1], L. V. E. Koopmans[11], AND K. Matthews[12]

[1] Department of Physics, University of California, Santa Barbara, CA 93106-9530, USA; suyu@physics.ucsb.edu
[2] Kavli Institute for Particle Astrophysics and Cosmology, Stanford University, 452 Lomita Mall, Stanford, CA 94035-4085, USA
[3] Argelander-Institut für Astronomie, Auf dem Hügel 71, 53121 Bonn, Germany
[4] Max-Planck-Institut für Mathematik, Vivatsgasse 7, 53111 Bonn, Germany
[5] ASTRON, Oude Hoogeveensedijk 4, 7991 PD Dwingeloo, The Netherlands
[6] Department of Physics, University of California Davis, 1 Shields Avenue, Davis, CA 95616, USA
[7] Excellence Cluster Universe, Technische Universität München, Boltzmannstr. 2, 85748 Garching, Germany
[8] Las Cumbres Observatory Global Telescope Network, 6740 Cortona Drive, Suite 102, Santa Barbara, CA 93117, USA
[9] Jodrell Bank Centre for Astrophysics, School of Physics and Astronomy, University of Manchester,
Turing Building, Oxford Road, Manchester M13 9PL, UK
[10] Large Binocular Telescope Observatory, University of Arizona, 933 North Cherry Avenue, Tucson, AZ 85721, USA
[11] Kapteyn Astronomical Institute, P.O. Box 800, 9700 AV Groningen, The Netherlands
[12] Caltech Optical Observatories, California Institute of Technology, Pasadena, CA 91125, USA

ABSTRACT

Measuring the relative mass contributions of luminous and dark matter in spiral galaxies is important for understanding their formation and evolution. The combination of a galaxy rotation curve and strong lensing is a powerful way to break the disk–halo degeneracy that is inherent in each of the methods individually. We present an analysis of the 10 image radio spiral lens B1933+503 at $z_1 = 0.755$, incorporating (1) new global very long baseline interferometry observations, (2) new adaptive-optics-assisted K-band imaging, and (3) new spectroscopic observations for the lens galaxy rotation curve and the source redshift. We construct a three-dimensionally axisymmetric mass distribution with three components: an exponential profile for the disk, a point mass for the bulge, and a Navarro–Frenk–White (NFW) profile for the halo. The mass model is simultaneously fitted to the kinematics and the lensing data. The NFW halo needs to be oblate with a flattening of $a/c = 0.33^{+0.07}_{-0.05}$ to be consistent with the radio data. This suggests that baryons are effective at making the halos oblate near the center. The lensing and kinematics analysis probe the inner $\sim$10 kpc of the galaxy, and we obtain a lower limit on the halo scale radius of 16 kpc (95% credible intervals). The dark matter mass fraction inside a sphere with a radius of 2.2 disk scale lengths is $f_{\rm DM,2.2} = 0.43^{+0.10}_{-0.09}$. The contribution of the disk to the total circular velocity at 2.2 disk scale lengths is $0.76^{+0.05}_{-0.06}$, suggesting that the disk is marginally submaximal. The stellar mass of the disk from our modeling is $\log_{10}(M_*/M_\odot) = 11.06^{+0.09}_{-0.11}$ assuming that the cold gas contributes $\sim$20% to the total disk mass. In comparison to the stellar masses estimated from stellar population synthesis models, the stellar initial mass function of Chabrier is preferred to that of Salpeter by a probability factor of 7.2.

Key words: galaxies: halos – galaxies: individual (B1933+503) – galaxies: kinematics and dynamics – galaxies: spiral – gravitational lensing: strong

Online-only material: color figures

1. INTRODUCTION

The discovery of flat rotation curves near and beyond the optical edge of galaxies provides strong evidence for the existence of dark matter (Rubin et al. 1978; Bosma 1978; van Albada & Sancisi 1986). Since then, observations of the cosmic microwave background, supernovae, galaxy clusters, weak lensing, baryon acoustic oscillations, and gravitational lens time delays indicate that our universe is well described by a model comprised of cold dark matter and dark energy (see, e.g., Komatsu et al. 2011; Suzuki et al. 2012; Mantz et al. 2010; Schrabback et al. 2010; Blake et al. 2011; Suyu et al. 2010). Even though the Λ-CDM model is successful at explaining the universe on large scales, the interplay between dark matter and baryons on galactic scales remains an open question.

N-body simulations of dark matter particles show that equilibrium dark matter halos have spherically averaged mass density profiles that are nearly universal (Navarro–Frenk–White, NFW; Navarro et al. 1996) and are typically triaxial in shape

(e.g., Jing & Suto 2002). The inclusion of baryons in simulations is challenging due to the large dynamical range in mass and uncertainties in the cooling and feedback mechanisms. Using a subset of the OverWhelmingly Large Simulations project (Schaye et al. 2010) that included various prescriptions of cooling and feedback, Duffy et al. (2010) found that the inner profile of galaxy-scale dark matter halos is very sensitive to the baryon physics. With weak stellar feedback from supernovae, the inner profiles tend to steepen and become more isothermal as a result of the high central baryon fractions that pull the dark matter toward the center. This "halo contraction" is also found in other studies (e.g., Blumenthal et al. 1986; Gnedin et al. 2004, 2011). On the other hand, with strong feedback from both supernovae and an active galactic nucleus, the inner profile is very similar to the NFW profile from dark-matter-only simulations. Measuring the inner profiles of dark matter halos therefore helps determine the kinds of baryonic processes that occur during galaxy formation and evolution.

Observationally, probing the inner profiles of dark matter halos with rotation curve data is difficult due to the disk–halo degeneracy (e.g., van Albada & Sancisi 1986; Dutton et al.

---

[13] Packard Research Fellow.

2005). Since the rotation curve primarily depends on the *total* enclosed mass within spherical radii, a heavy disk with a light halo and a light disk with a heavy halo can both be fit to the rotation curve. The degeneracy is prominent in models where the disk and halos have fixed parametric forms, and is reduced in self-consistent models where the halo shape changes in response to the presence of the disk (Amorisco & Bertin 2010). To circumvent the disk–halo degeneracy, some studies have assumed that the disk contributes maximally to the circular velocity. However, studies based on the Tully–Fisher relation or the central vertical velocity dispersion of disk stars have shown that disks tend to be submaximal (e.g., Courteau & Rix 1999; Bottema 1993; Bershady et al. 2011). To break the disk–halo degeneracy without resorting to maximal-disk assumptions, one needs to measure independently the relative mass contribution of the disk and the dark matter halo, or equivalently, the mass-to-light ratio (M/L) of the disk. Stellar population synthesis (SPS) models allow estimations of the stellar mass and hence the M/L of the disk. However, uncertainties in the stellar mass due to, for example, the unknown stellar initial mass function (IMF) limit the accuracy of this approach (e.g., Conroy et al. 2009). Therefore, disentangling the contributions of the disk and the halo to the rotation curve is key to understanding both the inner halo profile and the stellar IMF.

An effective way to overcome the disk–halo degeneracy is to combine rotation curves with strong gravitational lensing. If a spiral galaxy lies along the line of sight between the observer and a background source, the source can be strongly lensed into multiple images by the spiral galaxy (e.g., Treu 2010). While kinematics probe mass within spheres, strong lensing probes mass enclosed within cylinders (within the "Einstein radius," which is roughly the radial distance of the multiple images from the lens galaxy center). The combination of the two methods with different mass dependence breaks the disk–halo degeneracy. Spectroscopic and imaging surveys in recent years have substantially enlarged the sample of spiral lenses, totaling more than 20 now (e.g., Féron et al. 2009; Sygnet et al. 2010; Treu et al. 2011). The first few analyses of spiral lenses are already informing us about disk-maximality and the stellar IMFs in these systems (e.g., Koopmans et al. 1998; Maller et al. 2000; Trott et al. 2010; Dutton et al. 2011).

In this paper, we study B1933+503, a spiral gravitational lens at $z_1 = 0.755$ with 10 radio lensed images that was discovered by Sykes et al. (1998) in the Cosmic Lens All-Sky Survey (Myers et al. 2003; Browne et al. 2003). Previous modeling of the radio data by Cohn et al. (2001) tested power-law models for the combined dark and baryonic mass distribution of the lens. Here, we obtain new radio, infrared, and spectroscopic observations, and construct a three-component mass model (for the disk, bulge, and dark matter halo) that is simultaneously fitted to both the kinematics and lensing data. The analysis is very similar in spirit to the one presented by Dutton et al. (2011) on the lens SDSS J2141−0001, except we use an NFW instead of an isothermal profile to describe the dark matter halo. The aims of our study are (1) to measure the inner shape and profile of the dark matter halo, (2) to determine the relative contributions of the disk, bulge, and halo, and (3) to place constraints on the stellar IMF.

The paper is organized as follows. In Section 2, we present observations of the radio lens B1933+503. The alignment of the radio and near-infrared images is described in Section 3, and the lens light profile in the near-infrared image is measured in Section 4. The three-component mass model is outlined in Section 5, and the statistical framework for the analysis is described in Section 6. We present the kinematics-only and lensing-only results in Sections 7 and 8, respectively. We discuss the results and implications of the joint kinematics and lensing analysis in Section 9, before concluding in Section 10.

Throughout the paper, we assume a flat ΛCDM cosmology with $H_0 = 70$ km s^{-1} Mpc^{-1}, $\Omega_\Lambda = 1 - \Omega_m = 0.73$. In this cosmology, $1''$ corresponds to 7.5 kpc at the lens redshift and 8.7 kpc at the source redshift, which is measured in Section 2.5. Images of the lens system are north up and east left. Parameter constraints are given as the median values with uncertainties given by the 16th and 84th percentiles (corresponding to 68% credible intervals (CIs)) unless otherwise stated.

2. OBSERVATIONS

We obtained both lensing and kinematic observations of B1933+503 for constraining the lens mass distribution. We present the global very long baseline interferometry (VLBI) observations of the lensed radio source in Section 2.1, near-infrared imaging of the lens system in Sections 2.2 and 2.3, and spectroscopic data sets for obtaining the rotation curve of the lens galaxy and the source redshift in Sections 2.4 and 2.5. We describe the archival *Hubble Space Telescope* (*HST*) images in Section 2.6.

2.1. Radio Observations

We observed B1933+503 with the global VLBI array on 1998 November 27 at 1.7 GHz with a bandwidth of 16 MHz. We used 17 telescopes with 10 from the Very Long Baseline Array (VLBA) and 7 from the European VLBI Network (EVN). We adopt the center of component 4 of the lensed images as the phase center for the observations. Observations were conducted on a cycle of 6.5 minutes, with 1.5 minutes on a phase calibrator (B1954+51 = J1955+5131) followed by 5 minutes on the target source B1933+503. The exception was the Lovell telescope, which has a slower slew rate and for which every other observation of the phase calibrator was omitted, yielding a 1.5 minute + 11.5 minute cycle on the phase reference and target. The total observing time was nine hours, providing the good u–v coverage required for high dynamic range imaging and image fidelity. A single observation of 3C345 was obtained for fringe finding and flux calibration.

We reduce the data with the Astronomical Image Processing System[14] package using standard procedures. The images are iteratively CLEANed and self-calibrated (phase-only), before a single amplitude self-calibration solution is performed, to remove residual phase and amplitude errors. The final maps are produced using natural weighting of the visibilities and with a 10 Mλ taper to increase the sensitivity to the extended emission. The natural-weighting image has an rms noise level of 50 μJy beam^{-1} with a beam size of 5.7 × 2.7 mas at a position angle (P.A.) of −3°.22. The tapered image has an rms of 55 μJy beam^{-1} with a beam size of 20.1 × 16.5 mas at a P.A. of 60°.55. Figure 1 shows the final maps for each of the components in B1933+503, except for component 6, which is not detected.

The radio source being lensed has a compact core with two extended radio lobes on opposite sides of the core (Sykes et al. 1998; Nair 1998). The radio spectral indices make the identification of the images of the compact core unambiguous

---
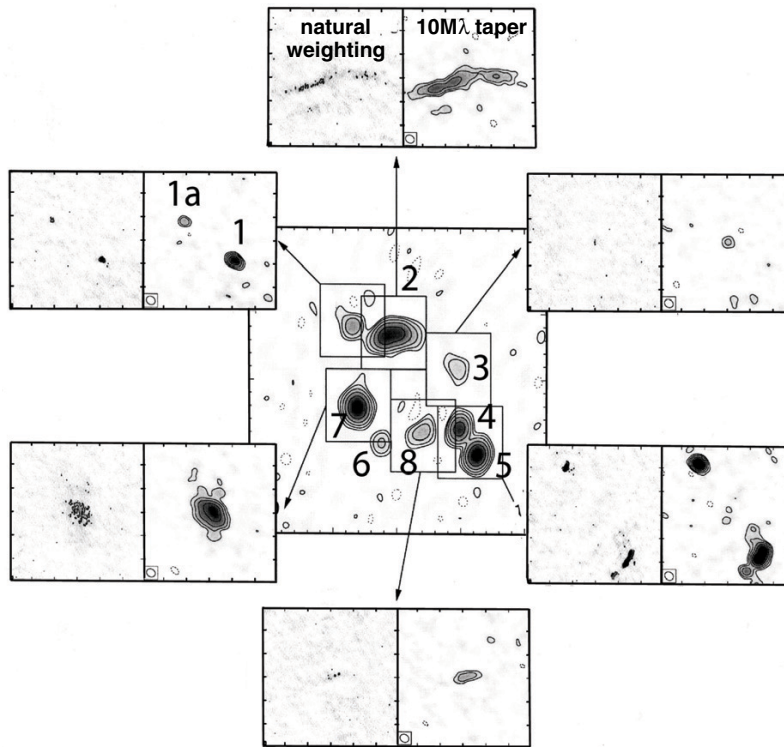
Figure 1. Global VLBI observations of B1933+503. Center: 1.7 GHz MERLIN observations of B1933+503 taken from Sykes et al. (1998). Contours are plotted at −3, 3, 6, 12, 24, 48 times the rms noise level of 150 μJy beam^{-1}. The beam size is 139 × 113 mas at a position angle of −13°.8. In each of the insets, the left and right panels show the 1.7 GHz global VLBI observations with natural weighting and with a 10 Mλ taper, respectively. In the left (right) panels, contours are plotted at −3, 3, 6, 12, 24, 48, 96 times the rms noise level of 50 (55) μJy beam^{-1}, and the beam size is 5.7 × 2.7 mas (20.1 × 16.5 mas) at a P.A. of −3°.22 (60°.55). Each of the global VLBI panels covers a 300 mas by 300 mas area with the tick marks separated by 50 mas.

(Sykes et al. 1998), and the flux densities of the core components showed little time variability (Biggs et al. 2000). Components 1, 3, 4, and 6 correspond to the images of the compact core, components 1a and 8 are the images of one of the lobes, and components 2, 5, and 7 correspond to the images of the other radio lobe. With component 2 counting as two (merging) images, B1933+503 is a spectacular 10 image radio lens.

We use components 1 and 4 to align the global VLBI data to the previous radio observations (with the Very Large Array, MERLIN, and VLBA) in Sykes et al. (1998) and Marlow et al. (1999). Table 1 lists the image positions for each of the components in the previous observations compiled by Cohn et al. (2001) and in the global VLBI data. The merging pair of images are denoted by components 2a and 2b. In the global VLBI data, several components (1, 4, 5, and 2a) have multiple intensity peaks, but some of their corresponding images (3 and 7) have only single peaks due to, e.g., scatter-broadening during propagation through the disk of the lens galaxy (e.g., Marlow et al. 1999; Norbury 2002). We adopt the flux-weighted average of the peak positions as the image positions and estimate the uncertainties from the separation of the peaks. We also set the positional uncertainty of component 7 and 2b to that of their counter image (component 5). For components that are spatially extended (1a and 8), the uncertainty is set to the geometric mean of the major and minor axis of the beam.

Cohn et al. (2001) also compiled flux ratios from Sykes et al. (1998), Nair (1998), and Biggs et al. (2000). We do not list or use the flux ratios because they could be systematically biased due to scattering and substructures in the lens. In fact, Kochanek & Dalal (2004) showed that the flux ratios in B1933+503 are anomalous due to substructures, and the constraints in B1933+503 lead to a relatively smooth, elliptical macro mass

model. Furthermore, Cohn et al. (2001) found that the exclusion of flux ratios had little effect on the main results of their mass models.

2.2. Keck AO-assisted NIRC2 Image

We observed B1933+503 with the adaptive-optics (AO) system at the Keck II telescope on 2005 July 31. We used the Kp filter (at 2.2 μm) on the Near Infrared Camera 2 (NIRC2) and took 33 dithered frames with a field of view of $10'' \times 10''$ that are each six co-adds of 30 s. The dithering allows good sky subtraction in the reduction. The natural tip-tilt reference star of magnitude $R \sim 16.4$ located at $\sim 21''.3$ southeast of B1933+503 and a sodium laser guide star were used to correct for atmospheric turbulence.

We use an IRAF-based algorithm to subtract the sky, remove bad pixels and cosmic rays, and produce weight maps for each frame. We use the weight maps and the DRIZZLE package (Fruchter & Hook 2002) to co-add the images together. We show in Figure 2 the drizzled NIRC2 image of the lens system. By comparing the positions of the three stars in the NIRC2 image to the corresponding stars in previous *HST* observations of the system (Section 2.6), we determine the pixel scale of the NIRC2 image to be 9.964 mas pixel^{-1}. The closest field star to B1933+503 ($\sim 2''.9$ away) in the combined NIRC2 image has an FWHM of ~ 57 mas.

2.3. Keck NIRC Image

In addition to the high-resolution NIRC2 image, we observed B1933+503 on 1996 July 31 with the Near Infrared Camera (NIRC; Matthews & Soifer 1994) at the Keck Observatory. The NIRC detector is 256 pixels on a side, with a pixel scale of

Table 1
Radio Image Positions

| Component ID | Cohn et al. (2001) | | | | Global VLBI | | | |
	System ID	ΔR.A. (arcsec)	ΔDecl. (arcsec)	Uncertainty (arcsec)	System ID	Δ R.A. (arcsec)	Δ Decl. (arcsec)	Uncertainty (arcsec)
1a	I	0.545	0.584	0.02	V	0.5538	0.5774	0.0042
8		−0.114	−0.335	0.02		−0.1219	−0.3266	0.0042
1	II	0.447	0.495	0.001	VI	0.4459	0.4945	0.001
3		−0.389	0.158	0.001		−0.3874	0.1635	0.0023
4		−0.397	−0.299	0.001		−0.3959	−0.2985	0.001
6		0.230	−0.387	0.005		. . .	. . .	. . .
5	III	−0.531	−0.497	0.005		. . .	. . .	. . .
7		0.398	−0.134	0.005		. . .	. . .	. . .
2a	IV	0.189	0.412	0.072	VII	0.1894	0.4129	0.04
2b		0.061	0.425	0.042		0.0737	0.4296	0.007
5		−0.522	−0.514	0.045		−0.5310	−0.4922	0.007
7		0.417	−0.130	0.049		0.3970	−0.1308	0.007

Notes. Column 1 lists the radio components as shown in Figure 1. Components 5 and 7 appear twice, with the peaks forming a two-image system, and the extended features forming a four-image system with the merging components 2a and 2b. Columns 2–5 are from Cohn et al. (2001), and Columns 6–9 are from the global VLBI observations in this paper. Columns 2 and 6 are the ID numbers for each multiple image system. Columns 3 and 7 (4 and 8) are the relative right ascensions (declinations) in the coordinate system of Cohn et al. (2001) where the origin is close to the lens center. Columns 5 and 9 are the estimated positional uncertainties.
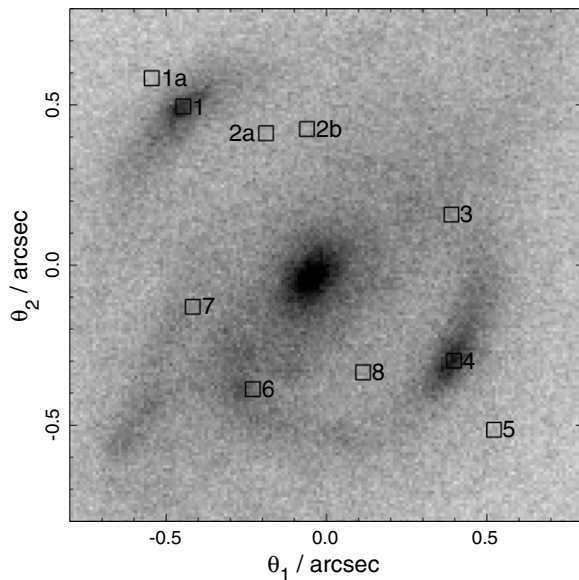
Figure 2. NIRC2 Kp image of B1933+503. The radio image positions from Cohn et al. (2001) are overlaid. The alignment of the NIRC2 and radio images is described in Section 3. The lensing arcs are associated with radio components 1, 3, 4, and 6, which are images of the compact core in the source. The arcs corresponding to components 3 and 6 are faint due to severe dust extinction in the plane of the spiral galaxy.

$0.''15$ pixel^{-1}. Thus, the field of view of the camera is $38.''4$ on a side, i.e., larger than the NIRC2 narrow camera field of view. The system was observed in both J and K bands, but the image quality of the J-band data was too poor to be useful. The K-band data consist of 59 exposures, each with an exposure time of one minute (five co-adds of 12 s each). The data were processed in a standard fashion, including steps to subtract the dark current, flatten the images, and subtract the sky. For each of the images, the flat field and sky frames were constructed from the frames observed directly before and after the image. The processed images were aligned by measuring the position of a star that appeared in each frame and then were co-added

to produce the final image. The photometric zero point of the NIRC data was determined through a comparison to the Two Micron All Sky Survey (2MASS; Skrutskie et al. 2006), which has K-band magnitudes for the two brightest stars in the image. The uncertainty in the photometric zero point is estimated to be 0.15 by comparing the magnitudes of the two stars. This incorporates the uncertainty due to the difference in throughput of the 2MASS and NIRC K-band filters, which we estimate to be $\lesssim 0.03$ by comparing the magnitude difference between the filters for several stars.

2.4. Keck ESI Spectroscopy

We observed B1933+503 using the Echelle Spectrograph and Imager (ESI; Sheinis et al. 2002) instrument at the Keck Observatory on 2002 June 6. The slit of width $1.''25$ was aligned along the major axis of the lens galaxy (P.A. = $138°$). The standard echellette mode yielded a spectral resolution with Gaussian width of $30 \, \mathrm{km \, s^{-1}}$. Five exposures of 1800 s each were taken under good seeing conditions of $0.''6$.

We reduce the data using the software EASI2D developed by D. J. Sand and T. Treu (Sand et al. 2004). We see prominent emission lines Hβ ($\lambda 4861$), [O II] ($\lambda 3726, \lambda 3729$), and [O III] ($\lambda 4959, \lambda 5007$) from the lens galaxy in the spectra. For each line, we set the center of the galaxy to the brightest pixel in the two-dimensional spectrum since measuring the center to much less than a pixel is difficult due to the presence of seeing. We then bin the spectrum in the spatial direction by a factor of three to increase the signal. Thus, the center of the galaxy should be well within the central binned spatial pixel of size $\sim 0.''5$. Any small offsets in the centroid are taken into account in the modeling in Section 7.3. The systemic velocity is difficult to measure from the data directly and is determined in the modeling (Section 7.3). Figure 3 is the rotation curve based on these lines.

2.5. Keck NIRSPEC Spectroscopy

We carried out infrared spectroscopic observations of the B1933+503 lensed source on 2005 September 9 with the Near Infrared Spectrometer (NIRSPEC; McLean et al. 1998) on the
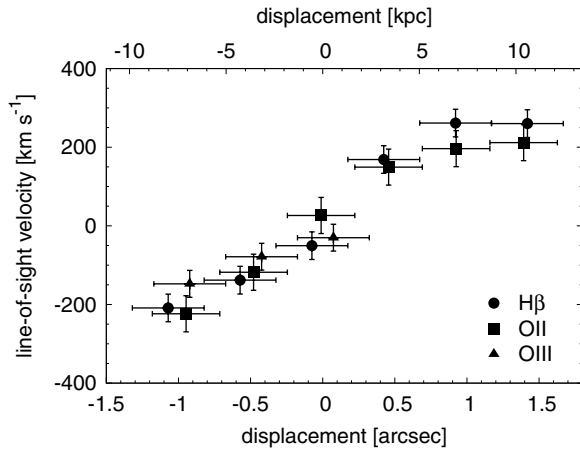
Figure 3. Rotation curve based on the observed emissions lines $H\beta$, [O II], and [O III] in the Keck ESI observations.

Keck II telescope. The data were taken through the NIRSPEC 6 and 7 filters (N6 and N7, respectively), which gave an approximate wavelength coverage of 1.56 to 2.02 μm and 2.08 to 2.52 μm, respectively. Each observation consisted of 4 × 300 s exposures that used dithering along the slit to improve the removal of the sky background during the reduction stage. The total exposure time was one hour through each filter. The slit was put at a position angle of 226°7 to cover the two strong infrared components from the lensed source. The standard star HD162208 was also observed four times each in N6 and N7 for calibration.

We reduce the data with a Python-based pipeline that removes cosmic rays, subtracts the sky, wavelength calibrates using the atmospheric skylines, and extracts a one-dimensional spectrum. Furthermore, we use the standard star HD162208 to correct for the response of the spectrograph. The reduced spectra for both filters are presented in the bottom panel of Figure 4, and the atmospheric transmission is shown in the top panel. The spectra are smoothed using a 7 pixel moving average with each point being weighted by the inverse variance associated with it. We identify a strong emission line in the N6 spectrum (bottom panel, left), but do not see any spectral features in the N7 spectrum (bottom panel, right). Therefore, we believe that the detected emission line is likely $H\alpha$ blended with two [N II] emission lines, corresponding to a source redshift of $z_s = 1.71 \pm 0.01$. The uncertainty in the redshift is conservative and accounts for the blending of the lines and also the contamination by atmospheric lines on both sides of the emission line.

We note that the strong emission line detected here has been previously reported by Biggs et al. (2000), based on an unpublished spectrum that was taken with the United Kingdom Infrared Telescope. Then the line was interpreted to be $H\beta$ at redshift 2.62 due to a second spectral feature that was believed to be $H\alpha$ in the K band. Our much better spectral resolution and higher sensitivity data do not detect the second emission line in N7, which would certainly have been detected if it were $H\alpha$ given the relative flux of the supposed $H\beta$ line in N6 and the noise level. We therefore rule out a redshift of 2.62 for the lensed source.

2.6. Archival HST Images

Archival *HST* images of B1933+503 in the F160W filter with the Near Infrared Camera and Multi-Object Spectrometer (NICMOS; Proposal ID: 9744; PI: Kochanek) and the F555W
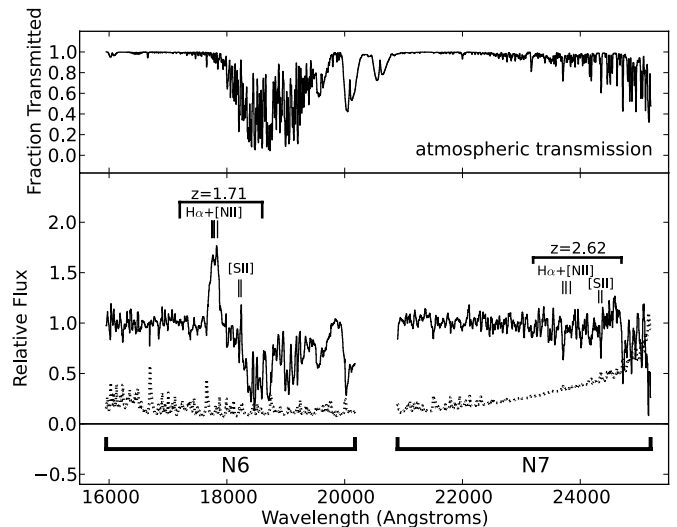
Figure 4. Spectra of the lensed source from NIRSPEC on Keck II in the N6 (left) and the N7 (right) filters are shown by the solid curves in the bottom panel. The rms noise spectra are the dotted curves. The spectra are smoothed using a 7 pixel moving average with each point being weighted by the inverse variance associated with it. The atmospheric transmission is shown in the top panel. In each of the N6 and N7 spectra, five emission lines (the first [N II] line, $H\alpha$, the second [N II] line and the two [S II] lines) are marked. The set in N6 is for a source redshift of $z_s = 1.71$, and the set in N7 is for $z_s = 2.62$ (with the broad line in N6 corresponding to $H\beta$). The absence of emission lines in N7 rules out the previously identified $z_s = 2.62$.

and F814W filters with the Wide Field and Planetary Camera 2 (WFPC2; Proposal ID: 9133; PI: Falco) are available. We used MULTIDRIZZLE[15] to combine the exposures in each filter and correct for geometric distortion. The F555W data were discarded due to the low signal-to-noise ratio (S/N). We oversampled the F814W and F160W images with MULTIDRIZZLE to the same pixel scale as the NIRC2 image, and show the color image composed of the three filters in Figure 5. The images of the lensed source in the plane of the lens galaxy (corresponding to radio components 3 and 6) suffer from dust extinction.

We use the stars in the WFPC2 F814W images to obtain the pixel scale of the NIRC2 image in Section 2.2 and the alignment of radio and NIRC2 images in Section 3. Furthermore, we use the F814W and F160W photometries in Section 4.3 to estimate the stellar mass of the lens galaxy (that incorporates the effects of dust) in Section 9.4.

3. RADIO AND NIRC2 IMAGE ALIGNMENT

In order to use both the radio image positions of the source and the NIRC2 image of the lens galaxy to constrain the lens mass distribution, we need to align the radio and the NIRC2 images. We assume that the two coordinate systems differ by a rotation and a translation. By aligning the stars in the NIRC2 images to the corresponding stars in the WFPC2 images with WCS information, we determine the north direction on the NIRC2 image, and consequently, the rotation between the radio and NIRC2 images. To determine the translational offset between the radio and NIRC2 images, we use the centroid positions of the two prominent arcs in the NIRC2 image, which we denote as P_1 and P_2. The separation between P_1 and P_2 and the angle of the segment connecting P_1 and P_2 match those of components 1 and 4 within 5 mas and 0°3, respectively. The matching of P_1 and

---

[15] MULTIDRIZZLE is a product of the Space Telescope Science Institute, which is operated by AURA for NASA.

Table 2
Lens Galaxy Light

	ΔR.A. (arcsec)	ΔDecl. (arcsec)	R_e (arcsec)	$n_{\rm sersic}$	q	ϕ (°)
Disk	0.040 ± 0.005	-0.036 ± 0.005	0.85 ± 0.05	$\equiv 1$	0.63 ± 0.06	138.0 ± 1.5
Bulge	0.040 ± 0.005	-0.036 ± 0.005	0.055 ± 0.006	$\equiv 1$	0.41 ± 0.02	147 ± 3

Notes. Sérsic profile parameters for the galaxy disk and bulge based on the NIRC2 image. Columns 2 and 3 are the relative right ascension and declination, respectively, in the coordinate system of Cohn et al. (2001) where the origin is close to the lens center. Column 4, 5, 6, and 7 are the effective radius, Sérsic index, axis ratio, and position angle of the Sérsic profile, respectively.
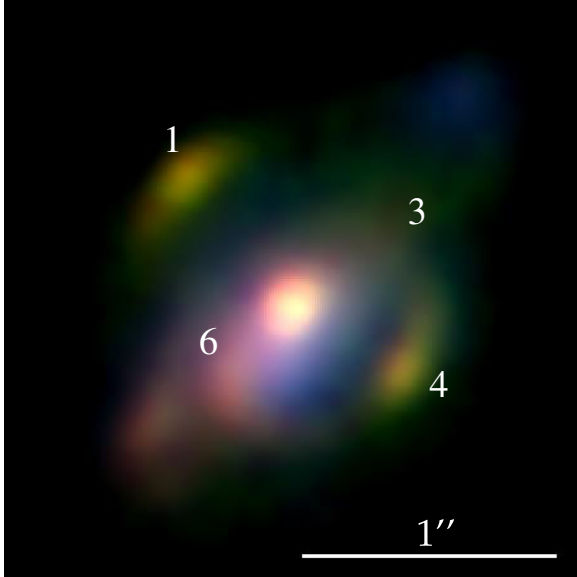
Figure 5. Color image from an RGB composite of the WFPC2 F814W, NICMOS F160W, and NIRC2 Kp images. The lensed arcs correspond to radio image components 1, 3, 4, and 6 of the compact core. Component 3 is barely visible and component 6 is reddened due to dust extinction in the plane of the spiral galaxy.

P_2 to components 1 and 4 agrees with previous identifications of features in the F160W image of Marlow et al. (1999). We construct the coordinate translation from the NIRC2 to the radio image by mapping the midpoint of the segment connecting P_1 and P_2 to the midpoint of the segment connecting components 1 and 4. We show in Figure 2 the superposition of the radio and NIRC2 data sets.

The positions P_1 and P_2 of the arcs in the Keck infrared image can be determined with an accuracy of 5 mas. We add this systematic alignment uncertainty to the positional uncertainty of the galaxy centroid in the mass modeling. We also incorporate the uncertainty in the rotation between the NIRC2 and radio image (0.°3) to the uncertainty in the P.A. of the lens galaxy.

Having determined the transformation from the NIRC2 image to the radio observations, all coordinates values are reported with respect to the system used in Table 1 for the remainder of the paper.

4. LENS GALAXY LIGHT DISTRIBUTION

In this section, we describe the steps taken to model the light profile of the lens galaxy in the NIRC2 image.

4.1. PSF

A model of the point-spread function (PSF) is needed to extract the intrinsic light profile of the lens galaxy without atmospheric and instrumental blurring. We use the star that is $\sim 2.''9$ northwest of B1933+503 in the observed field as a model of the PSF. Previous works have shown that field stars serve as good PSF models, especially for spatially extended objects (e.g., Marshall et al. 2007; Suyu et al. 2009).

4.2. Lens Light Profile

To model the lens galaxy light, we use the GALFIT package (Peng et al. 2002). We mask out the lensing arcs and the spiral arm-like features in the southeast region of the galaxy. Optionally, we also mask out the central region of the galaxy. We find that the galaxy is well described by two exponential disk profiles with a common centroid (or a single exponential disk profile, if the central region was masked out). Specifically, we employ Sérsic profiles with index $n_{\rm sersic} \equiv 1$ that correspond to exponential disks and also fit a uniform background for the sky. One of the Sérsic profiles corresponds to the disk of the galaxy and the other is centrally localized with a small effective radius ($\sim 0.''05$).[16] We identify this latter component as a bulge, although it could also be a bar given the limited resolution. We estimate the uncertainties on the Sérsic parameters based on differences in the best-fit parameter values for different choices of masks. This systematic uncertainty dominates the statistical uncertainty of the fit. For the galaxy centroid, we include the systematic uncertainty of 5 mas (from the alignment of NIRC2 and radio data) which dominates the overall positional uncertainty. Table 2 lists the best-fit values for the mask containing the lensed arcs and spiral arm features.

We see in Figure 6 that the two-component Sérsic model reproduces the overall structure of the lens galaxy light, and the background fit yields uniform sky residuals. The reduced χ^2 is 1.03 in the fitting region. The residuals show, apart from the three strong lensing arcs (corresponding to radio components 1, 4, and 6 in Figure 2), some small-scale features that could be spiral arms or tidal features in the lens galaxy. In Sections 7.3 and 8.2, we account for the effects of these residual features in the mass modeling by adding systematic uncertainties to the line-of-sight velocities and the radio image positions.

4.3. Lens Photometry

The photometry of the lens is required for estimating the stellar mass from SPS models in Section 9.4. To obtain the integrated K-band magnitudes for the disk and the bulge based on the exponential profiles in the previous section, we first determine the photometric zero point of the NIRC2 image by calibrating it with the low-resolution NIRC K-band image. We then integrate the model light profiles and list in Table 3 the K-band magnitudes of the disk and the bulge, where the estimated uncertainty comes from calibration, difference in

---

[16] The effective radius of the central component remains small ($< 0.''07$) even when the Sérsic index is allowed to vary between 1 and 4.
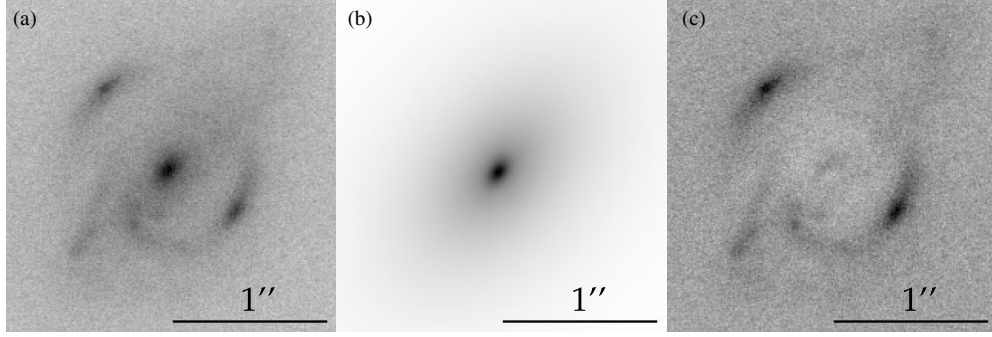
Figure 6. Lens galaxy light. (a) NIRC2 Kp image, (b) modeled lens galaxy light based on two exponential disk profiles for the galaxy disk and bulge, (c) residual image.

Table 3
Lens Photometry

	WFPC2 F814W	NICMOS F160W	NIRC2 K
Disk	19.0 ± 0.3	17.5 ± 0.3	18.5 ± 0.3
Bulge	23.0 ± 0.3	22.1 ± 0.3	22.9 ± 0.3

Note. Magnitudes are in the AB system.

throughput of NIRC2 Kp and NIRC K filters, and variations between different arc masks.

The *HST* images have significantly lower S/N than the NIRC2 image. Therefore, we use the structural parameters (axis ratio, position angle, and effective radius) of the exponential profiles from the NIRC2 image (listed in Table 2) to obtain the integrated magnitudes in F814W and F160W with GALFIT. We use the nearest field star to approximate the PSF. The separation of the arcs and the lens light is more difficult in these low S/N images, and we conservatively adopt an uncertainty of 0.3 mag from various choices in the arc masks. The integrated magnitudes for the disk and the bulge are listed in Table 3.

5. GALAXY MASS COMPONENTS

We decompose the spiral galaxy into three mass components: a disk of stars and gas, a bulge, and a dark matter halo. We now briefly describe the mass distribution for each component.

5.1. Disk

We assume that the disk of stars and gas in the galaxy is thin and circularly symmetric. Furthermore, we assume that there is a constant M/L throughout the disk. Hence, the exponential profile for the light in Section 4.2 implies that the profile for the elliptical surface mass density of the projected (inclined) disk is

$$\Sigma_d^P(R') = \Sigma_{d,0} \exp[-R'/R_d], \tag{1}$$

where $\Sigma_{d,0}$ is the normalization of the disk (set by the M/L), R_d is the scale radius of the disk, and R' is given in terms of the coordinates x', y' along the major/minor axes centered on the galaxy by

$$R'^2 = x'^2 + (y'/q_d)^2. \tag{2}$$

The axis ratio q_d is related to the inclination angle i of the disk by

$$q_d = \cos i, \tag{3}$$

where $i = 0°$ corresponds to a face-on disk.

In terms of the radial coordinates in the plane of the disk, $R = \sqrt{x^2 + y^2}$, the surface mass density is

$$\Sigma_d(R) = \Sigma_{d,0} \, q_d \, \exp[-R/R_d], \tag{4}$$

where the extra factor of q_d in the normalization ensures that an inclined disk and a face-on disk have the same total mass. The scale radius R_d is related to the effective radius (the half-light radius in Table 2, which is also the half-mass radius with a constant M/L by $R_d = R_e/1.678$.

For gravitational lensing, the quantity of interest is the dimensionless surface mass density,

$$\kappa_d(R') = \Sigma_d^P(R')/\Sigma_{crit} \tag{5}$$

$$= \kappa_{d,0} \, \exp[-R'/R_d], \tag{6}$$

where

$$\Sigma_{crit} = \frac{c_l^2}{4\pi G} \frac{D_s}{D_d D_{ds}}, \tag{7}$$

$\kappa_{d,0}$ is the disk strength, c_l is the speed of light, and G is the gravitational constant. The distances D_d, D_s, and D_{ds} are angular diameter distances to the lens, to the source, and between the lens and the source, respectively.

5.2. Bulge

The galaxy light fitting suggests that we can model the bulge as a point mass, since the effective radius of the corresponding Sérsic profile is very small compared to the radial range of positions spanned by the lensed images ($\sim0\overset{''}{.}3$–$0\overset{''}{.}8$) and most of the points in the rotation curve.

5.3. Dark Matter Halo

We assume an NFW profile (Navarro et al. 1996) with a triaxial shape (Jing & Suto 2002) for the dark matter halo. The three-dimensional density distribution is given by

$$\rho_h(r) = \frac{\rho_{h,0}}{(r/r_{h,0})(1 + r/r_{h,0})^2}, \tag{8}$$

where

$$r^2 = c^2 \left(\frac{x^2}{a^2} + \frac{y^2}{b^2} + \frac{z^2}{c^2} \right), \quad a \leqslant b \leqslant c. \tag{9}$$

The parameters a, b, and c describe the triaxial shape of the halo. The orientation of the dark matter halo as seen by a distant observer can be described by two angles ϑ and φ. Following Oguri et al. (2003), we choose (ϑ, φ) as the polar angle of the

observer's line-of-sight direction in the halo coordinate system (x, y, z) (see Figure 1 of Oguri et al. 2003). With this definition, Equations (1) and (2) of Oguri et al. (2003) relate the coordinates in the frame of the halo (x, y, z) to the coordinates of the distant observer (x', y', z').

The two-dimensional surface mass density of the projected triaxial halo is elliptical, and the axis ratio (q_h) and position angle (ϕ_h) of the ellipse can be calculated given the values for a/c, b/c, ϑ, and φ (Oguri et al. 2003). We use the Einstein radius for the corresponding spherical mass model, $R_{h,E}$, to characterize the strength of the halo since lensing can robustly measure this quantity. The Einstein radius is the radius of the ring that is formed by a point source lying perfectly behind a spherical halo with strength $R_{h,E}$. The normalization $\rho_{h,0}$ is related to the Einstein radius $R_{h,E}$ by

$$\rho_{h,0} = A \begin{cases} [1 - \log(2)]^{-1} & \text{if } \tilde{R}_{h,E} = 1 \\ \left[\log\left(\frac{\tilde{R}_{h,E}}{2}\right) + \frac{2}{\sqrt{1 - \tilde{R}_{h,E}^2}} \right. \\ \left. \cdot \operatorname{arctanh}\left(\sqrt{\frac{1 - \tilde{R}_{h,E}}{1 + \tilde{R}_{h,E}}}\right) \right]^{-1} & \text{if } \tilde{R}_{h,E} < 1 \\ \left[\log\left(\frac{\tilde{R}_{h,E}}{2}\right) + \frac{2}{\sqrt{\tilde{R}_{h,E}^2 - 1}} \right. \\ \left. \cdot \arctan\left(\sqrt{\frac{\tilde{R}_{h,E} - 1}{\tilde{R}_{h,E} + 1}}\right) \right]^{-1} & \text{if } \tilde{R}_{h,E} > 1 \end{cases}, \quad (10)$$

where

$$A = \frac{\Sigma_{crit}}{4 r_{h,0} D_d} \tilde{R}_{h,E}^2, \quad (11)$$

and $\tilde{R}_{h,E} = R_{h,E}/r_{h,0}$. Both $R_{h,E}$ and $r_{h,0}$ are in arcseconds (which can be easily converted to, e.g., kiloparsecs, with the angular diameter distance to the lens, D_d).

5.4. External Shear

For the lensing analysis in Section 8, we also include an external shear component with strength γ_{ext} and a position angle of ϕ_{ext}. A shear angle of $\phi_{ext} = 0$ corresponds to an elongation of the images in the east–west direction.

5.5. Combined Mass Model

For simplicity, we impose a symmetry condition on the model. To be precise, we require that the centroids of the three components coincide and that the total mass distribution is three-dimensionally axisymmetric. In particular, the NFW profile is either prolate ($a = b$) or oblate ($b = c$). Based on the symmetry assumptions and the axis ratio and P.A. of the projected disk (in Table 2), the orientation of the halo is $(\vartheta, \varphi) = (50 \pm 5°, 145 \pm 3°)$.

Cohn et al. (2001) found that the orientation of the quadrupole moment of their lens model (one-component total mass profile and external shear) agrees with the position angle of the lens galaxy within $\sim 5°$. This implies that the position angle of the projected total mass distribution is aligned with the light distribution of the galaxy. We confirm the alignment by modeling the lens system using a pseudoisothermal elliptic mass distribution (Kassiola & Kovner 1993) in the presence of external shear. The alignment of the projected total mass distribution and the light implies that the NFW halo is oblate (in the inner region probed by lensing) since a prolate halo would lead to a $\sim 90°$ difference in the position angles of the projected mass and the light distributions.

Table 4
Priors on Model Parameters

Description	Parameter	Prior
Centroid in θ_1	$\theta_{1,c}$	$G(-0\rlap{.}''040, 0\rlap{.}''005)$
Centroid in θ_2	$\theta_{2,c}$	$G(-0\rlap{.}''036, 0\rlap{.}''005)$
Disk axis ratio	q_d	$G(0.63, 0.06)$
Disk strength	$\kappa_{d,0}$	$U(0, \infty)$
Disk scale radius	R_d	$G(0\rlap{.}''51, 0\rlap{.}''03)$
Bulge mass	M_b	$U(0, \infty)$
Halo flattening	$a/c = a/b$	$U(0.25, 1)$
Halo orientation angle	ϑ	$G(50°, 5°)$
Halo orientation angle	φ	$G(145°, 3°)$
Halo Einstein radius	$R_{h,E}$	$U(0, \infty)$
Halo scale radius	$r_{h,0}$	$U(0\rlap{.}''1, 8'') \equiv U(0.75, 60)\,\mathrm{kpc}$
External shear strength	γ_{ext}	$U(0, 0.3)$
External shear angle	ϕ_{ext}	$U(0, 2\pi)$

Notes. $G(\mu, \sigma)$ is a Gaussian distribution with mean μ and standard deviation σ. $U(a, b)$ is a uniform distribution between boundaries a and b. In cases where $b = \infty$, the upper boundary is set to a real number that corresponds to masses $\gtrsim 10^{13} M_\odot$, i.e., larger than galaxy-scale masses.

We impose Gaussian priors on (1) the centroid of the total mass distribution, (2) the projected axis ratio and scale radius of the disk, and (3) the orientation of the NFW halo, based on the observed light profile in Table 2. The position angle of the projected disk is set by the orientation of the NFW halo (based on the axisymmetry assumption). We impose uniform priors on the remaining parameters and summarize the priors in Table 4. While all these priors are imposed for the lens modeling, some are not needed for the kinematics, such as the external shear.[17] In total, we have 13 mass parameters: 6 with Gaussian priors, and 7 "free" parameters with uniform priors.

6. BAYESIAN ANALYSIS

We use Bayesian analysis to infer the mass model parameters. In particular, we sample the posterior probability distribution function (PDF) of the 13 mass parameters $\boldsymbol{\eta}$, which is given by

$$P(\boldsymbol{\eta}|\boldsymbol{d}) = \frac{\overbrace{P(\boldsymbol{d}|\boldsymbol{\eta})}^{\text{likelihood}} \overbrace{P(\boldsymbol{\eta})}^{\text{prior}}}{\underbrace{P(\boldsymbol{d})}_{\text{evidence}}}, \quad (12)$$

where $\boldsymbol{d}$ is the data. The expressions for the likelihoods of the kinematics and the lensing data are in Sections 7.3 and 8.2, respectively. The prior $P(\boldsymbol{\eta})$ is given by

$$P(\boldsymbol{\eta}) = \prod_{i=1}^{13} P(\eta_i), \quad (13)$$

where η_i is the ith parameter and $P(\eta_i)$ is either a Gaussian or a uniform distribution as described in Section 5.5. The Bayesian evidence is used for comparing different forms of models, which does not concern us in this paper since we consider only one form of mass model: an exponential disk, a point mass bulge, and an oblate NFW halo.

---

[17] B1933+503 is not in any obvious galaxy group or cluster, so any external shear is likely to come from structures that are not dynamically associated with the lens system.

7. ROTATION CURVE MODELING

In this section, we describe the modeling of the galaxy mass distribution based on the rotation curve constraints. We assume that the gas in the disk (from which we observed the emission lines for the rotation curve) is in circular orbits, and use the circular velocities of the mass model to predict the line-of-sight velocities for constructing the likelihood of the kinematics data. We then sample the posterior PDF of the kinematics data.

7.1. Circular Velocities

For a test mass in the plane of the disk at a radius R from the center, its circular velocity $v_c(R)$ has three contributions:

$$v_c^2 = v_b^2 + v_d^2 + v_h^2, \qquad (14)$$

where v_b, v_d, and v_h are the circular velocities of the bulge, disk, and halo mass distributions, respectively.

For the point-mass bulge, the rotational velocity contribution v_b takes on a simple form

$$v_b^2 = \frac{GM_b}{R}, \qquad (15)$$

where G is the gravitational constant and M_b is the mass of the bulge.

The contribution of the disk also has an analytic expression in terms of Bessel functions I_0, K_0, I_1, and K_1 (e.g., Binney & Tremaine 1987):

$$v_d^2 = 4\pi G\Sigma_c R_d y^2 (I_0(y)K_0(y) - I_1(y)K_1(y)), \qquad (16)$$

where Σ_c is the central surface mass density of the disk ($\equiv \kappa_{d,0}\Sigma_{crit}q_d$), R_d is the scale radius of the disk, y is related to the radial distance R by $y = R/2R_e$, and R_e is the effective radius of the mass profile of the disk.

For the halo component, we follow Binney & Tremaine (1987) and integrate the oblate spheroidal three-dimensional mass density $\rho(m)$ with $m^2 = x^2/q_h^2 + y^2 + z^2$ to obtain the circular velocity:

$$v_h^2 = 4\pi G q_h \int_0^R m^2 \frac{\rho(m)}{\sqrt{R^2 - m^2(1 - q_h^2)}} dm, \qquad (17)$$

where $q_h = a/c$ is the flattening of the dark matter halo. For the NFW mass density (Equation (8)), we numerically compute the integral in Equation (17).

7.2. Predicted Rotation Curve

To model the rotation curve, we follow van der Marel & van Dokkum (2007) to obtain the predicted line-of-sight velocities from the circular velocities which incorporate the effects of the disk inclination, slit, and seeing.

The line-of-sight velocity in the absence of the slit and seeing at a point (x', y') on the sky (with $(x', y') = (0, 0)$ at the center of the galaxy and x' along the major axis of the lens galaxy) is

$$v_{los}(x', y') = \frac{x}{R} \sin(i) v_c(R), \qquad (18)$$

where $\boldsymbol{R} = (x, y)$ is the corresponding coordinate in the plane of the disk with $x = x'$, $y = y'/\cos i$, and $R = |\boldsymbol{R}|$.

We weight v_{los} by the modeled galaxy light, and convolve with both a Gaussian PSF with FWHM of $0.''6$ and a square top-hat function of size $W \times P$ (for slit of width W and pixel scale P) for each (binned) spatial pixel along the slit. The resulting weighted and convolved velocity is the predicted line-of-sight velocity v_{los}^{pred} at the corresponding spatial pixel.
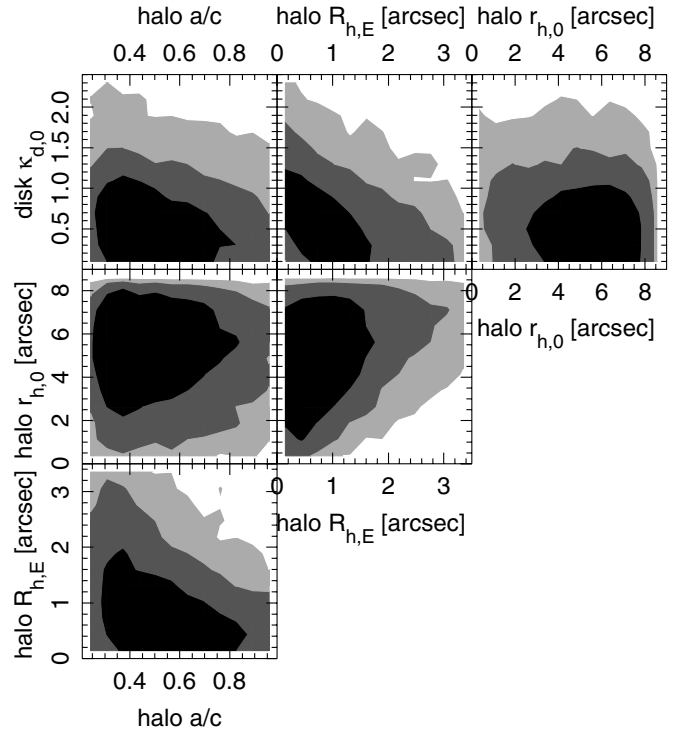
Figure 7. Marginalized posterior PDF for the halo flattening a/c, halo Einstein radius $R_{h,E}$, halo scale radius $r_{h,0}$, and disk strength $\kappa_{d,0}$ based on only the rotation curve data. The three shaded areas show the 68.3%, 95.4%, and 99.7% credible regions. The disk–halo degeneracy is illustrated in the top middle panel: higher $R_{h,E}$ corresponds to lower $\kappa_{d,0}$.

7.3. Kinematics Analysis and Results

The uncertainties of the data points in the rotation curve of Figure 3 are only statistical. We include a systematic uncertainty of $40\,\mathrm{km\,s^{-1}}$ (which is comparable to the statistical uncertainty) to account for deviations from our assumptions of the smooth axisymmetric mass model, slight offset (if any) of the galaxy centroid in the rotation curve, and the unknown systemic velocity. We explore a range of values for the systemic velocity and choose the value that optimizes the rotation curve fitting. We add the statistical and the systematic uncertainty in quadrature to obtain the final uncertainty on the line-of-sight velocity. The amount of systematic uncertainty is set such that the rotation curve can be modeled with a reduced $\chi^2 \sim 1$. The inclusion of the systematic uncertainty is crucial for not underestimating the uncertainty on the resulting mass model parameters.

The likelihood for the rotation curve data is

$$P(\boldsymbol{d}_D|\boldsymbol{\eta}) = \frac{1}{Z_D} \exp\left[-\frac{1}{2}\sum_{i=1}^{N_D} \frac{(v_{los,i}^{obs} - v_{los,i}^{pred})^2}{\sigma_i^2}\right], \qquad (19)$$

where N_D is the number of data points ($= 15$), $v_{los,i}^{obs}$ is the observed line-of-sight velocity of data point i, $v_{los,i}^{pred}$ is the predicted line-of-sight velocity from our model and observational setup, σ_i is the uncertainty in the velocity, and Z_D is the normalization given by

$$Z_D = (2\pi)^{N_D/2} \prod_{i=1}^{N_D} \sigma_i. \qquad (20)$$

We use MULTINEST (Feroz & Hobson 2008; Feroz et al. 2009) to sample the posterior PDF of the 13 model parameters. Figure 7

shows the resulting constraints on four of the parameters: halo flattening a/c, halo Einstein radius $R_{h,E}$, halo scale radius $r_{h,0}$, and disk strength $\kappa_{d,0}$. The disk–halo degeneracy appears as the anti-correlation between the disk strength ($\kappa_{d,0}$) and the halo Einstein radius ($R_{h,E}$): the more massive the disk, the less massive the halo, and vice versa. The halo scale radius is poorly constrained. Furthermore, the kinematics data provide little information on the halo shape.

Figure 8 shows the predicted rotation curve of the most probable mass distribution with a reduced $\chi^2 = 1.0$ based on the kinematics data. The bulge contributes very little to the mass of the system, consistent with the small effective radius observed for the bulge light distribution. At small (large) radii, the disk (dark matter halo) dominates in the enclosed mass.

8. LENS MODELING

In this section, we discuss the properties of our three-component mass model based on the lensing constraints.

8.1. Lensing Deflection Angles

We briefly describe how to obtain the deflection angles for the three mass components in our model. The deflection angles are used to solve for the predicted radio image positions that are needed for constructing the likelihood of the lensing data.

8.1.1. Disk

The lensing deflection angles for an elliptical mass component following an exponential disk profile has no analytical form. Hence, to model the stellar disk component, we employ a "chameleon profile" mimicking the mass profile of an exponential disk whose deflection angles are analytical. This profile is inspired by the chameleon profile used in Maller et al. (2000). We use the following approximation for the dimensionless surface mass density of the disk:

$$\kappa_d(R') = \kappa_{d,0} \exp[-R'/R_d] \tag{21}$$

$$\approx \kappa_{d,0} s_1 \left[\frac{1}{\sqrt{R'^2 + s_2^2}} - \frac{1}{\sqrt{R'^2 + s_3^2}} \right], \tag{22}$$

where $s_1 = 4.6849 R_d$, $s_2 = 1.1720 R_d$, and $s_3 = 1.4518 R_d$. The projected enclosed mass within radius $\tilde{R}'$ for the chameleon profile agrees with that of the exponential profile within 2% for the range of radii spanned by the lensed images ($\tilde{R}' = 0.6 R_d$–$1.6 R_d$). Each term in the square brackets in Equation (22) is in the form of a pseudoisothermal elliptic mass distribution whose deflection angles can be computed analytically (Kassiola & Kovner 1993).

8.1.2. Bulge

The bulge is modeled as a point mass, and the deflection angle has a simple closed form (e.g., Schneider et al. 2006)

$$\alpha(\xi) = \frac{4G}{c_1^2} \frac{M_b}{\xi}, \tag{23}$$

where G is the gravitational constant, c_1 is the speed of light, M_b is the mass of the bulge, and ξ is the impact parameter (i.e., the distance between the light ray and the point mass on the lens plane).
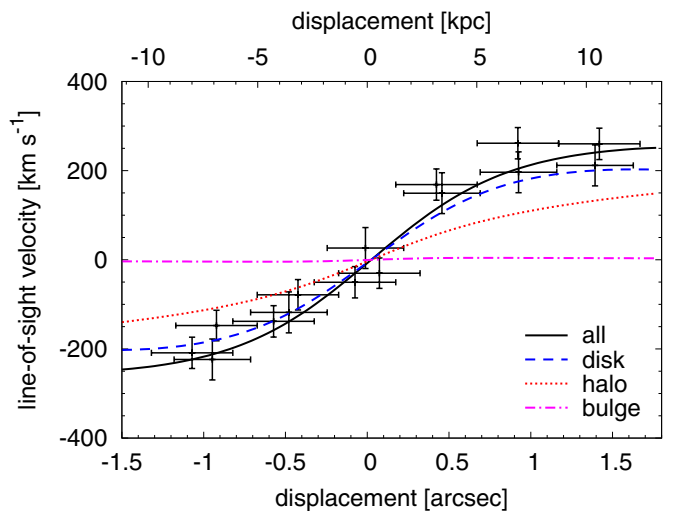
Figure 8. Rotation curve of the most probable mass model based on kinematics data only. The contributions from the disk (blue dashed), halo (red dotted), and bulge (magenta dot-dashed) are indicated. Most of the mass is in the disk and the dark matter halo.

(A color version of this figure is available in the online journal.)

8.1.3. Dark Matter Halo

We refer the reader to Oguri et al. (2003) for the lensing properties of the triaxial NFW halo in Equations (8) and (9). The projected surface mass density of the halo is elliptical, and the deflection angles can be computed numerically.

### 8.2. Lensing Analysis and Results

We use the radio image positions listed in Table 1 to constrain the mass model parameters. We add a positional uncertainty of 10 mas in quadrature to the uncertainties in the table to account for systematic effects such as the residual features in the lens galaxy light fit (Section 4.2), presence of substructure (e.g., Chen et al. 2007), and scatter-broadening through the disk of the lens (e.g., Marlow et al. 1999; Biggs et al. 2004). The lensing arcs in the NIRC2 images could in principle be used in addition to the radio image positions to constrain the lens mass distribution; however, these arcs (especially the one associated with components 3 and 6) in practice suffer from dust extinction. Only the F160W image of the *HST* data has sufficient S/N to be used for dust correction, and Suyu et al. (2009) showed that dust correction based on two bands are prone to systematic effects. Therefore, we do not include the dust-affected NIRC2 arcs for constraining the mass distribution.

The likelihood of the radio image positions is

$$P(d_L|\eta) = \frac{1}{Z_L} \exp \left[-\frac{1}{2} \sum_{j=1}^{N_{sys}} \sum_{i=1}^{N_{im}^j} \frac{\left| \theta_{i,j}^{obs} - \theta_{i,j}^{pred}(\eta) \right|^2}{\sigma_{i,j}^2} \right], \tag{24}$$

where N_{sys} is the number of multiply imaged systems, N_{im}^j is the number of multiple images in system j, $\theta_{i,j}^{obs}$ is the observed image position, $\theta_{i,j}^{pred}(\eta)$ is the modeled image position, $\sigma_{i,j}$ is the uncertainty in the observed image position, and Z_L is the normalization given by

$$Z_L = (2\pi)^{N_L/2} \prod_{j=1}^{N_{sys}} \prod_{i=1}^{N_{im}^j} \sigma_{i,j} \tag{25}$$
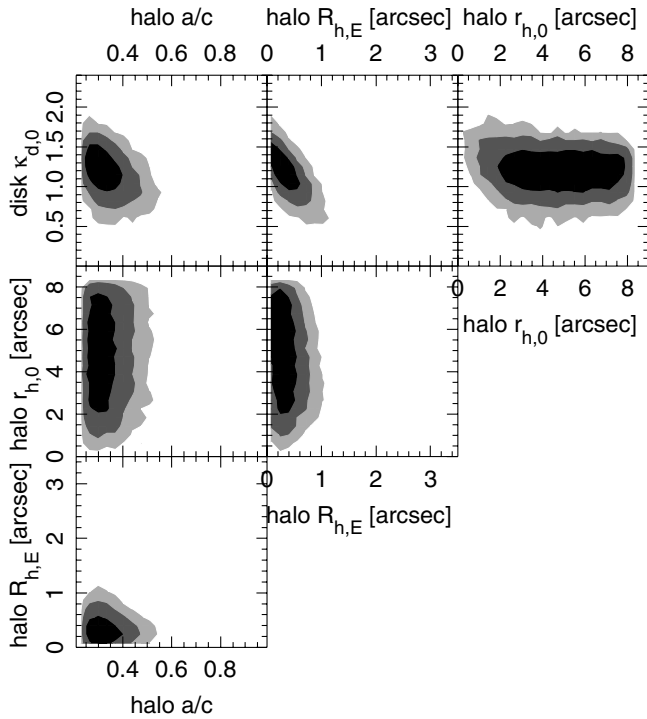
Figure 9. Marginalized posterior PDF for the halo flattening a/c, halo Einstein radius $R_{\rm h,E}$, halo scale radius $r_{\rm h,0}$, and disk strength $\kappa_{\rm d,0}$ based on only the lensing data. The three shaded areas show the 68.3%, 95.4%, and 99.7% credible regions. The panels are plotted on the same scales as in Figure 7 for comparison.

with

$$N_{\rm L} = \sum_{j=1}^{N_{\rm sys}} N_{\rm im}^{j}. \tag{26}$$

The source position for each system of multiple images is needed to predict the image positions. We model the source position as the weighted average of the mapped source positions from the observed image positions and the deflection angles from the mass distribution. Specifically, for each image system, we take the average of the mapped source position $\boldsymbol{\beta}_i$ weighted by $\sqrt{\mu_i}/\sigma_i$, where μ_i and σ_i are, respectively, the modeled magnification and the positional uncertainty of image i.[18] In doing so, we have in effect marginalized the source position parameters by approximating the lensing likelihood as having a delta function at the weighted source position for each image system.

We model the three-component mass distribution of the spiral galaxy based on the lensing data with GLEE ("Gravitational Lens Efficient Explorer"), a software developed by A. Halkola & S. H. Suyu.[19] For a set of mass model parameter values, GLEE computes the values of the lensing likelihood in Equation (24) and the prior in Equation (13); these are the two ingredients needed to obtain the posterior PDF in Equation (12). As in

the kinematics analysis, we use MULTINEST (Feroz & Hobson 2008; Feroz et al. 2009) to sample the posterior PDF.

Figure 9 shows the resulting constraints on the same parameters as those in Figure 7. The degeneracy between the disk strength and the Einstein radius of the dark matter halo is visible, though not as strong as in the case of the kinematics-only analysis. The halo is highly flattened ($a/c \sim 0.3$). The flattening is degenerate with the disk strength as shown in the top left panel: a flattened halo is less massive and requires a more massive disk. The flattening is also degenerate with the halo Einstein radius: massive halos with high $R_{\rm h,E}$ need to be more flattened to reproduce the overall ellipticity of the projected mass as constrained by the lensing data. The scale radius of the dark matter halo is not constrained, as expected since lensing only probes the distribution in the radial range spanned by the images, i.e., $\sim 0\rlap{.}''5$, or ~ 4 kpc. Nonetheless, a small value of $\lesssim 1''$ is rejected by the data at 95% CI.

The most probable lensing model (with highest posterior PDF) has a reduced $\chi^2 = 0.9$. We show in Figure 10 the critical curves (solid) and caustics (dashed) of the most probable lensing model. The open symbols are the observed image positions, and the solid symbols are the modeled source positions. The figure illustrates the configuration of the 10 image system in relation to its three-component source (the source positions are clustered into three groups). The first group of sources is outside the astroid caustics and produces components 1a and 8. The second group is inside the astroid caustics and produces components 1, 3, 4, and 6. The third group is near a fold of the caustics and produces components 2, 5, and 7.

9. COMBINING KINEMATICS AND LENSING

In this section, we present results on the mass distribution for the spiral galaxy based on the kinematics and lensing data sets. Since the two data sets are independent, the likelihood is

$$P(\boldsymbol{d}_{\rm D}, \boldsymbol{d}_{\rm L}|\boldsymbol{\eta}) = P(\boldsymbol{d}_{\rm D}|\boldsymbol{\eta})\, P(\boldsymbol{d}_{\rm L}|\boldsymbol{\eta}), \tag{27}$$

where the kinematics and lensing likelihoods on the right-hand side are given by Equations (19) and (24), respectively. Figure 11 shows the result of MULTINEST sampling of the posterior. The reduced χ^2 of the joint data set is 0.8. The marginalized parameters with 68% CI are listed in Table 5.

9.1. Breaking the Disk–Halo Degeneracy

Although the kinematics constraints are significantly weaker than the lensing constraints, the $\kappa_{\rm d,0}$–$R_{\rm h,E}$ panel (top middle) in Figure 11 shows that the kinematics and lensing contours are tilted at different angles. Thus, the combination of the two in principle breaks the disk–halo degeneracy. In the case of B1933+503, most of the constraints on the mass distribution come from the lensing data: the 10 radio images, which both span a large range of radii and have positional uncertainties of only a few mas, provide a strong leverage in discerning contributions from the disk, bulge, and halo. This is in contrast to typical lenses with only two or four images which result in stronger disk–halo degeneracies (e.g., Trott et al. 2010). On the other hand, the S/N of the rotation curve data for B1933+503 is only modest given the high lens redshift of $z_1 = 0.755$. Nonetheless, the kinematics data in B1933+503 are informative in excluding the high disk masses allowed by lensing, which has interesting consequences that are discussed in Section 9.4.

A disk is considered to be maximal if the fractional contribution to the circular velocity of the disk at $2.2\,R_{\rm d}$ is

---

[18] Our tests using analytic mass profiles show that the weighted source positions and the optimized source positions give consistent constraints on the mass parameters. Since the computation time of the weighted source positions is an order of magnitude shorter than that of the optimized source positions and the deflection angles of the oblate NFW halo are computationally expensive (due to the numerical integration), we use the weighted source positions.

[19] The software models the mass distribution in gravitational lenses using image positions (Halkola et al. 2008) or extended images with pixelated source (Suyu et al. 2006). We refer the reader to Suyu & Halkola (2010) for an example of each approach.

Table 5
Marginalized Parameters (68% CI)

Disk q_d	Disk $\kappa_{d,0}$	Bulge M_b ($10^{10}\,M_\odot$)	Halo a/c	Halo q_h	Halo ϕ_h (°)	Halo $R_{h,E}$ (arcsec)	Halo $r_{h,0}$ (arcsec)	γ_{ext}	ϕ_{ext} (°)
0.53 ± 0.03	1.1 ± 0.2	1.6 ± 0.3	$0.33^{+0.07}_{-0.05}$	0.67 ± 0.04	137 ± 2	0.4 ± 0.2	5 ± 2	0.02 ± 0.01	103 ± 14

Notes. The marginalized model parameters for the three-component mass distribution constrained by lensing and kinematics. Columns 1–2 are the projected disk axis ratio and strength. Column 3 is the bulge mass. Columns 4–8 are the halo flattening, projected axis ratio, projected position angle, Einstein radius, and scale radius. Columns 9–10 are the external shear strength and position angle.
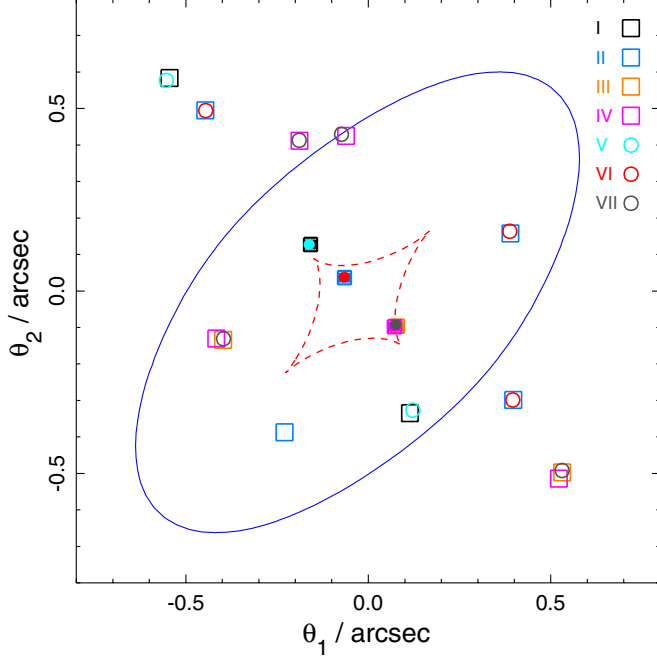
Figure 10. Critical curves (solid) and caustics (dashed) of the most probable model based on lensing data only. The open symbols are the observed image positions that are labeled according to Table 1: squares are the images positions in Cohn et al. (2001), and circles are the global VLBI image positions. The corresponding solid symbols are the modeled source positions. The three groups of source positions, which have one group outside the astroid caustics (with image multiplicity of 2) and two groups inside the caustics (with image multiplicity of 4), form the 10 image system. The model reproduces the observed image positions to within 0″.02, except for the merging components 2a and 2b (in systems IV and VII), which are reproduced to within 0″.06 due to the higher positional uncertainty from the high magnification.

$v_d(2.2\,R_d)/v_{tot}(2.2\,R_d) = 0.85 \pm 0.1$ (Sackett 1997). Based on our lensing and kinematics model, B1933+503 has $v_d(2.2\,R_d) = 248^{+22}_{-26}\,\mathrm{km\,s^{-1}}$ and $v_{tot}(2.2\,R_d) = 326 \pm 8\,\mathrm{km\,s^{-1}}$. In comparison to the Milky Way's circular velocity at the position of the sun, $v_c(R_0) = (219 \pm 20)\,R_0/(8\,\mathrm{kpc})\,\mathrm{km\,s^{-1}}$ (Reid et al. 1999), the spiral galaxy in B1933+503 is significantly more massive. The resulting disk contribution in B1933+503 of $v_d(2.2\,R_d)/v_{tot}(2.2\,R_d) = 0.76^{+0.05}_{-0.06}$ suggests that the disk is marginally submaximal.

9.2. Shape and Profile of the Dark Matter Halo

In the first column of Figure 11, we see that the dark matter halo in B1933+503 is oblate with $a/c = 0.33^{+0.07}_{-0.05}$ in order to fit to the lensing observations. The axis ratio of the projected surface mass density of the halo is 0.67 ± 0.04, which is slightly rounder than the axis ratio of projected disk of 0.53 ± 0.03. It appears that only projected mass distributions of the lens with axis ratios of ∼0.6 are consistent with the lensing data. If we consider the subset of the MULTINEST sample with $a/c \sim 0.5$
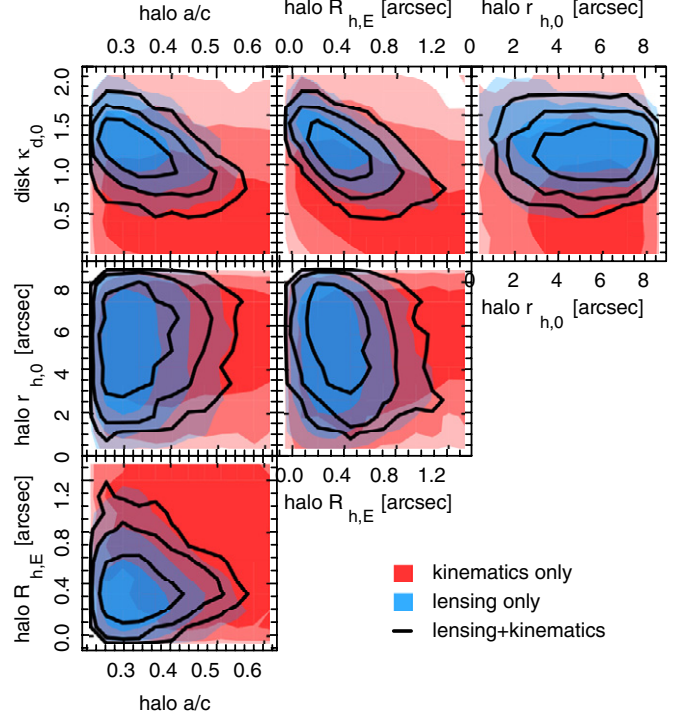

Figure 11. Marginalized posterior PDF for the halo flattening a/c, halo Einstein radius $R_{h,E}$, halo scale radius $r_{h,0}$, and disk strength $\kappa_{d,0}$ based on kinematics only (red), lensing only (blue), and joint lensing and kinematics (black). The three shaded areas show the 68.3%, 95.4%, and 99.7% credible regions.

(which corresponds to a projected axis ratio of ∼0.75), then the lensing reduced χ^2 increases from 0.8 to 2.4 due to misfits in systems II, V, VI, and VII in Table 1. The global VLBI data with better positional accuracies and, in particular, the four-image systems II and VI enforce the high ellipticity in the projected surface mass density and hence the highly oblate halo. The high ellipticity is robust against assumptions on the dark matter halo profile. In particular, when we replace the NFW halo with either a singular or cored isothermal profile, the radio data still require a high ellipticity for the halo.

N-body simulations of dark matter halos indicate that the halos are typically triaxial and the axis ratio between the short and long axis (i.e., a/c in our notation) is ∼0.3–0.9 (95% CI) for halo masses of 10^{11}–$10^{12}\,M_\odot$ (e.g., Bett et al. 2007; Macciò et al. 2008). Simulations with baryons find that the central galaxy tends to make the triaxial halo essentially oblate and less flattened (e.g., Abadi et al. 2010). Our study of B1933+503 with the resulting $a/c \sim 0.3$ for the oblate NFW halo suggests that baryons are effective at making the halo oblate in the inner regions of the galaxy.

Since the kinematics and lensing data probe the inner ∼1″ = 7.5 kpc of the galaxy, it is not surprising that the scale radius
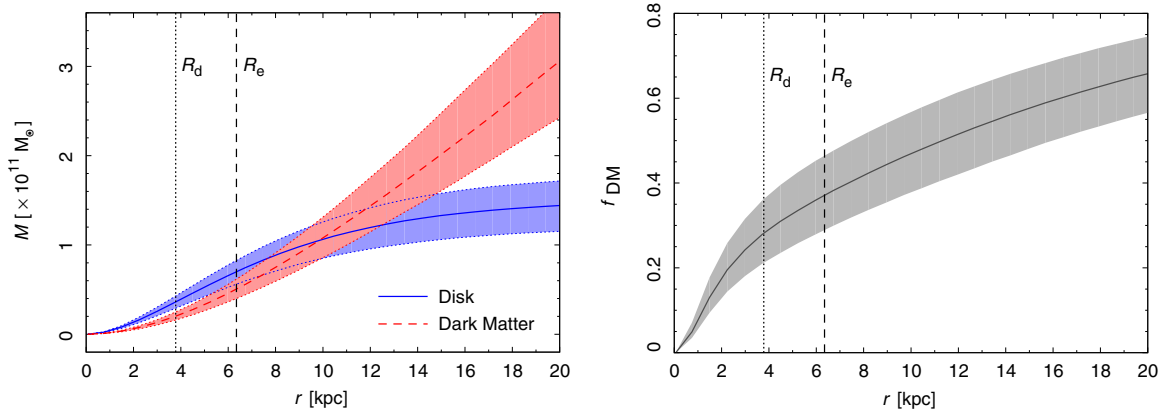
Figure 12. Masses and dark matter mass fractions from the lensing and kinematics modeling. Left panel: spherical enclosed mass of the disk and halo components. The bulge is modeled as a point mass of $(1.6 \pm 0.3) \times 10^{10} \, M_\odot$. Right panel: the dark matter mass fraction within a sphere. The dotted (dashed) vertical line is the scale (effective) radius of the disk.

(A color version of this figure is available in the online journal.)

$r_{h,0}$ of the dark matter halo in our model (where the density transitions from $\rho \sim r^{-1}$ to r^{-3}) is not constrained but has a lower limit of $2''.1 = 16 \, \text{kpc}$ (95% CI). The virial radius is difficult to extrapolate from the model given the uncertain scale radius. For galaxies with total mass of $\sim 10^{12} \, M_\odot$ (applicable to B1933+503), typical virial radii are $\sim 250 \, \text{kpc}$. This implies a concentration of $\lesssim 16$ that is consistent with concentration–mass relations for galaxy-scale halos (e.g., Macciò et al. 2008; Duffy et al. 2010). To better constrain $r_{h,0}$, a rotation curve that extends to larger radii is needed.

9.3. Dark Matter Mass Fraction

From our three-component model of the galaxy, we can determine the fraction of dark matter as a function of radius by integrating the mass enclosed within spherical radii. Since we employ a parameterized model and the parameters of the model are constrained by the lensing and kinematics data, the enclosed mass can be computed for all radii. At small and large radii where there is no (or low S/N) data, the enclosed mass is effectively extrapolated based on the form of the parametrized model and the measured values of the mass parameters. The left panel in Figure 12 shows the mass enclosed for the disk and the dark matter halo. The bulge, which is unresolved and modeled as a point, has mass $M_b = (1.6 \pm 0.3) \times 10^{10} \, M_\odot$ for all radii. In the inner 10 kpc of the galaxy, we see that the disk dominates in mass, and beyond that, the dark matter halo dominates.

The right panel shows the dark matter mass fraction within a sphere of radius r. The rise in the dark matter fraction is similar to the analysis of the spiral lens SDSS J2141−0001 by Dutton et al. (2011). The dark matter mass fraction within 2.2 disk scale lengths for B1933+503 is $f_{DM,2.2} = 0.43^{+0.10}_{-0.09}$. Within the effective radius, the mass fraction is $f_{DM,e} = 0.37^{+0.09}_{-0.08}$, which is consistent with the ranges of values found in previous lensing and kinematics analyses of early-type galaxies (e.g., Auger et al. 2010a; Barnabè et al. 2011).

9.4. Implications for the IMF

The shapes of the low- and high-mass end of the stellar IMF are difficult to determine observationally since low-mass stars are intrinsically faint and high-mass stars are low in abundance. In this section, we describe the estimation of the stellar mass in B1933+503 based on SPS models for Chabrier (2003) and Salpeter (1955) IMFs. We compare these masses
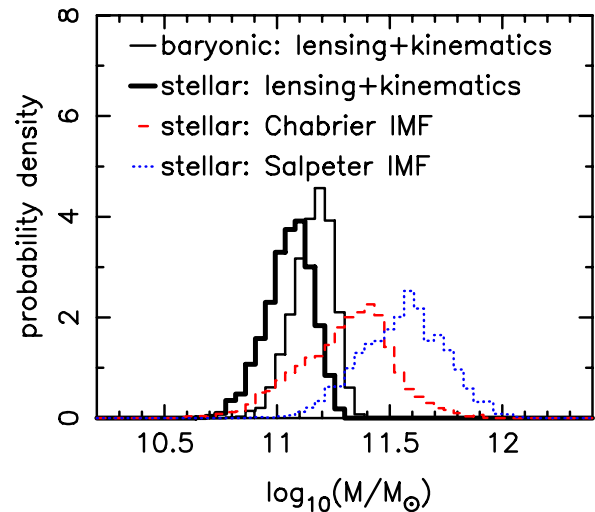
Figure 13. Comparison of the disk mass from the lensing and kinematics analysis, and the stellar mass from photometry and stellar population synthesis with Chabrier or Salpeter IMFs. A Chabrier-like IMF is preferred to a Salpeter-like IMF by a factor of 7.2 when a $20\% \pm 10\%$ contribution in mass from the cold gas is assumed.

(A color version of this figure is available in the online journal.)

to the independently measured disk mass from lensing and kinematics to learn about the IMF.

Using the broadband photometries in Table 3, we follow Auger et al. (2009) to infer the stellar mass for the disk based on composite SPS models from Bruzual & Charlot (2003). These models have been employed in many studies including Sloan Digital Sky Survey (SDSS) galaxies (e.g., Kauffmann et al. 2003; Gallazzi et al. 2005) and spiral lens analyses similar to ours (e.g., Dutton et al. 2011). Dust extinction (intrinsic) is taken into account in these models, and our multiband photometries allow a good handle on dust with only a small broadening of uncertainties (e.g., Bell & de Jong 2001). Our inference of the stellar mass provides uncertainties that incorporate parameter degeneracies in the stellar population models (e.g., between age and metallicity). In Figure 13, we plot the inferred stellar mass in red-dashed (blue-dotted) assuming a Chabrier (Salpeter[20]) IMF. These two IMFs cover the range applicable to spiral galaxies (Bell & de Jong 2001).

---

[20] We use $0.1 \, M_\odot$ as the lower mass limit for the Salpeter IMF.

The lensing and kinematics analysis provides an independent measurement of the total disk mass of $\log_{10}(M_{\rm disk}/M_\odot) = 11.17^{+0.08}_{-0.10}$ that includes stars and gas (thin solid curve in Figure 13). To extract the stellar mass contribution, we assume that the cold gas accounts for 20% ± 10% of the total mass (e.g., Dutton & van den Bosch 2009) and is distributed like the stars. This provides an upper limit on the mass contribution of the gas to the disk (in comparison to scenarios where the gas is more extended than the stars). For each sample in the posterior PDF of the disk mass, we draw a random number f from a Gaussian distribution centered on 0.2 with a standard deviation of 0.1 that is truncated between [0,1], and subtract the fraction f from the total disk mass. The gas-subtracted disk mass from the lensing and kinematics model is $\log_{10}(M_*/M_\odot) = 11.06^{+0.09}_{-0.11}$, and the distribution is shown by the thick solid curve in Figure 13.

Comparing the thick solid curve to the dashed and dotted curves in the figure, we see that our mass model of B1933+503 favors a Chabrier-like IMF. We can quantitatively rank the two IMFs by computing the Bayesian evidence which is the integral under the product of the PDF from lensing and kinematics (thick solid) and the PDF from the SPS (dashed or dotted). The ratio of the Bayesian evidence for Chabrier to Salpeter is 7.2; in other words, the probability of the IMF being Chabrier is 7.2 times higher than the probability of the IMF being Salpeter for B1933+503.

Using the Chabrier IMF, we obtain the rest-frame stellar mass-to-light ratio of the disk to be $M_*/L_{\rm V} = (0.6 \pm 0.3)M_\odot/L_{\rm V,\odot}$. By passively evolving to $z = 0$, we obtain the present-day stellar mass-to-light ratio of $M_*/L_{\rm V} = (1.7^{+1.3}_{-0.9})M_\odot/L_{\rm V,\odot}$, in agreement with typical values found for local galaxies (e.g., Trott et al. 2010; van de Ven et al. 2010; Courteau & Rix 1999; van der Kruit & Freeman 2011, and references therein).

Our finding of a preference toward a Chabrier-like IMF for the spiral galaxy is in agreement with the results in Dutton et al. (2011) and Ferreras et al. (2010). Nonetheless, studies of massive elliptical galaxies favor Salpeter-like IMFs (e.g., Treu et al. 2010; Auger et al. 2010b; van Dokkum & Conroy 2010; Spiniello et al. 2011). This supports a non-universal IMF for galaxies that is dependent on mass and/or Hubble type.

10. CONCLUSIONS

We disentangled the distributions of baryons and dark matter in the spiral galaxy B1933+503 by using the newly acquired global VLBI observations, AO-assisted NIRC2 imaging, rotation curve, and source redshift. We constructed an axisymmetric three-component mass model for the galaxy with an exponential disk, a point mass to approximate the unresolved bulge, and an NFW dark matter halo. Parameters of this model were constrained by a combined lensing and kinematics analysis. Based on this study, we conclude the following.

1. The image positions of the radio source span a range of radii and provide strong constraints on the three-component mass distribution of the lens.
2. The fractional contribution of the disk to the total circular velocity at $2.2\,R_{\rm d}$ is $0.76^{+0.05}_{-0.06}$, suggesting that the disk is marginally submaximal.
3. The oblate dark matter halo needs to be highly flattened with $a/c \sim 0.3$ in order to fit to the radio observations.
4. The lensing and kinematics data sets probe the inner ∼10 kpc region of the mass distribution and place a lower limit of 16 kpc (95% CI) for the scale radius of the NFW halo.

5. The dark matter mass fraction inside a sphere increases as a function of radius. The mass fraction within $2.2\,R_{\rm d}$ is $f_{\rm DM,2.2} = 0.43^{+0.10}_{-0.09}$, and within the effective radius is $f_{\rm DM,e} = 0.37^{+0.09}_{-0.08}$.
6. The total stellar mass of the disk based on the lensing and kinematics data sets is $\log_{10}(M_*/M_\odot) = 11.06^{+0.09}_{-0.11}$, assuming that the cold gas is distributed like the stars.
7. Based on the lensing and kinematics measurement of the disk mass, the Chabrier IMF is preferred to the Salpeter IMF by a probability factor of 7.2.

The sample of spiral lenses has been growing rapidly in recent years thanks to dedicated surveys (e.g., Marshall et al. 2009; Sygnet et al. 2010; Treu et al. 2011). While most of the lenses do not have sources that are radio loud, spatially extended lensed images can also be used to constrain the mass distribution (e.g., Dutton et al. 2011). The combined lensing and kinematics modeling methods we have developed are general, and important insights into the interactions between baryons and dark matter in the formation and evolution of spiral galaxies can be derived from a sample of lenses using these techniques.

REFERENCES

Abadi, M. G., Navarro, J. F., Fardal, M., Babul, A., & Steinmetz, M. 2010, MNRAS, 407, 435
Amorisco, N. C., & Bertin, G. 2010, A&A, 519, A47
Auger, M. W., Treu, T., Bolton, A. S., et al. 2009, ApJ, 705, 1099
Auger, M. W., Treu, T., Bolton, A. S., et al. 2010a, ApJ, 724, 511
Auger, M. W., Treu, T., Gavazzi, R., et al. 2010b, ApJ, 721, L163
Barnabè, M., Czoske, O., Koopmans, L. V. E., Treu, T., & Bolton, A. S. 2011, MNRAS, 415, 2215
Bell, E. F., & de Jong, R. S. 2001, ApJ, 550, 212
Bershady, M. A., Martinsson, T. P. K., Verheijen, M. A. W., et al. 2011, ApJ, 739, L47
Bett, P., Eke, V., Frenk, C. S., et al. 2007, MNRAS, 376, 215
Biggs, A. D., Browne, I. W. A., Jackson, N. J., et al. 2004, MNRAS, 350, 949
Biggs, A. D., Xanthopoulos, E., Browne, I. W. A., Koopmans, L. V. E., & Fassnacht, C. D. 2000, MNRAS, 318, 73

Binney, J., & Tremaine, S. (ed.) 1987, Galactic Dynamics (Princeton, NJ: Princeton Univ. Press)

Blake, C., Davis, T., Poole, G. B., et al. 2011, MNRAS, 415, 2892

Blumenthal, G. R., Faber, S. M., Flores, R., & Primack, J. R. 1986, ApJ, 301, 27

Bosma, A. 1978, PhD thesis, Groningen Univ., Groningen, The Netherlands

Bottema, R. 1993, A&A, 275, 16

Browne, I. W. A., Wilkinson, P. N., Jackson, N. J. F., et al. 2003, MNRAS, 341, 13

Bruzual, G., & Charlot, S. 2003, MNRAS, 344, 1000

Chabrier, G. 2003, PASP, 115, 763

Chen, J., Rozo, E., Dalal, N., & Taylor, J. E. 2007, ApJ, 659, 52

Cohn, J. D., Kochanek, C. S., McLeod, B. A., & Keeton, C. R. 2001, ApJ, 554, 1216

Conroy, C., Gunn, J. E., & White, M. 2009, ApJ, 699, 486

Courteau, S., & Rix, H.-W. 1999, ApJ, 513, 561

Duffy, A. R., Schaye, J., Kay, S. T., et al. 2010, MNRAS, 405, 2161

Dutton, A. A., Brewer, B. J., Marshall, P. J., et al. 2011, MNRAS, 417, 1621

Dutton, A. A., Courteau, S., de Jong, R., & Carignan, C. 2005, ApJ, 619, 218

Dutton, A. A., & van den Bosch, F. C. 2009, MNRAS, 396, 141

Féron, C., Hjorth, J., McKean, J. P., & Samsing, J. 2009, ApJ, 696, 1319

Feroz, F., & Hobson, M. P. 2008, MNRAS, 384, 449

Feroz, F., Hobson, M. P., & Bridges, M. 2009, MNRAS, 398, 1601

Ferreras, I., Saha, P., Leier, D., Courbin, F., & Falco, E. E. 2010, MNRAS, 409, L30

Fruchter, A. S., & Hook, R. N. 2002, PASP, 114, 144

Gallazzi, A., Charlot, S., Brinchmann, J., White, S. D. M., & Tremonti, C. A. 2005, MNRAS, 362, 41

Gnedin, O. Y., Ceverino, D., Gnedin, N. Y., et al. 2011, arXiv:1108.5736

Gnedin, O. Y., Kravtsov, A. V., Klypin, A. A., & Nagai, D. 2004, ApJ, 616, 16

Halkola, A., Hildebrandt, H., Schrabback, T., et al. 2008, A&A, 481, 65

Jing, Y. P., & Suto, Y. 2002, ApJ, 574, 538

Kassiola, A., & Kovner, I. 1993, ApJ, 417, 450

Kauffmann, G., Heckman, T. M., White, S. D. M., et al. 2003, MNRAS, 341, 33

Kochanek, C. S., & Dalal, N. 2004, ApJ, 610, 69

Komatsu, E., Smith, K. M., Dunkley, J., et al. 2011, ApJS, 192, 18

Koopmans, L. V. E., de Bruyn, A. G., & Jackson, N. 1998, MNRAS, 295, 534

Macciò, A. V., Dutton, A. A., & van den Bosch, F. C. 2008, MNRAS, 391, 1940

Maller, A. H., Simard, L., Guhathakurta, P., et al. 2000, ApJ, 533, 194

Mantz, A., Allen, S. W., Rapetti, D., & Ebeling, H. 2010, MNRAS, 406, 1759

Marlow, D. R., Browne, I. W. A., Jackson, N., & Wilkinson, P. N. 1999, MNRAS, 305, 15

Marshall, P. J., Hogg, D. W., Moustakas, L. A., et al. 2009, ApJ, 694, 924

Marshall, P. J., Treu, T., Melbourne, J., et al. 2007, ApJ, 671, 1196

Matthews, K., & Soifer, B. T. 1994, in Astronomy with Arrays, The Next Generation, ed. I. S. McLean (Astrophysics and Space Science Library, Vol. 190; London: Springer), 239

McLean, I. S., Becklin, E. E., Bendiksen, O., et al. 1998, Proc. SPIE, 3354, 566

Myers, S. T., Jackson, N. J., Browne, I. W. A., et al. 2003, MNRAS, 341, 1

Nair, S. 1998, MNRAS, 301, 315

Navarro, J. F., Frenk, C. S., & White, S. D. M. 1996, ApJ, 462, 563

Norbury, M. 2002, PhD thesis, Univ. Manchester, Manchester

Oguri, M., Lee, J., & Suto, Y. 2003, ApJ, 599, 7

Peng, C. Y., Ho, L. C., Impey, C. D., & Rix, H.-W. 2002, AJ, 124, 266

Reid, M. J., Readhead, A. C. S., Vermeulen, R. C., & Treuhaft, R. N. 1999, ApJ, 524, 816

Rubin, V. C., Thonnard, N., & Ford, W. K., Jr. 1978, ApJ, 225, L107

Sackett, P. D. 1997, ApJ, 483, 103

Salpeter, E. E. 1955, ApJ, 121, 161

Sand, D. J., Treu, T., Smith, G. P., & Ellis, R. S. 2004, ApJ, 604, 88

Schaye, J., Dalla Vecchia, C., Booth, C. M., et al. 2010, MNRAS, 402, 1536

Schneider, P., Kochanek, C. S., & Wambsganss, J. (ed.) 2006, Gravitational Lensing: Strong, Weak and Micro (Berlin: Springer)

Schrabback, T., Hartlap, J., Joachimi, B., et al. 2010, A&A, 516, A63

Sheinis, A. I., Bolte, M., Epps, H. W., et al. 2002, PASP, 114, 851

Skrutskie, M. F., Cutri, R. M., Stiening, R., et al. 2006, AJ, 131, 1163

Spiniello, C., Koopmans, L. V. E., Trager, S. C., Czoske, O., & Treu, T. 2011, MNRAS, 417, 3000

Suyu, S. H., & Halkola, A. 2010, A&A, 524, A94

Suyu, S. H., Marshall, P. J., Auger, M. W., et al. 2010, ApJ, 711, 201

Suyu, S. H., Marshall, P. J., Blandford, R. D., et al. 2009, ApJ, 691, 277

Suyu, S. H., Marshall, P. J., Hobson, M. P., & Blandford, R. D. 2006, MNRAS, 371, 983

Suzuki, N., Rubin, D., Lidman, C., et al. 2012, ApJ, 746, 85

Sygnet, J. F., Tu, H., Fort, B., & Gavazzi, R. 2010, A&A, 517, A25

Sykes, C. M., Browne, I. W. A., Jackson, N. J., et al. 1998, MNRAS, 301, 310

Treu, T. 2010, ARA&A, 48, 87

Treu, T., Auger, M. W., Koopmans, L. V. E., et al. 2010, ApJ, 709, 1195

Treu, T., Dutton, A. A., Auger, M. W., et al. 2011, MNRAS, 417, 1601

Trott, C. M., Treu, T., Koopmans, L. V. E., & Webster, R. L. 2010, MNRAS, 401, 1540

van Albada, T. S., & Sancisi, R. 1986, Phil. Trans. R. Soc. A, 320, 447

van de Ven, G., Falcón-Barroso, J., McDermid, R. M., et al. 2010, ApJ, 719, 1481

van der Kruit, P. C., & Freeman, K. C. 2011, ARA&A, 49, 301

van der Marel, R. P., & van Dokkum, P. G. 2007, ApJ, 668, 738

van Dokkum, P. G., & Conroy, C. 2010, Nature, 468, 940